The Astronomical Journal, 125:2568–2583, 2003 May

HIGH-RESOLUTION MID-INFRARED OBSERVATIONS OF VERY YOUNG STELLAR OBJECTS IN NGC 1333

L. M. Rebull,[1,2] D. M. Cole,[3] K. R. Stapelfeldt,[3] and M. W. Werner[3]

Received 2002 December 23; accepted 2003 February 11

ABSTRACT

We observed 22 young stellar objects in the region of NGC 1333 by using the mid-infrared camera MIRLIN. NGC 1333 (in the Perseus OB2 molecular cloud complex) is a relatively well studied region, but not at high spatial resolution in the mid-infrared. MIRLIN's 0.″5 spatial resolution allows us to look for source extension and multiplicity and to place new constraints on spectral energy distributions. We report here new detections of eight objects at mid-IR wavelengths. We find one object, SVS 12, that may be extended or multiple, and we confirm multiplicity in SVS 16. We find a new companion to ASR 107. We are able to classify six objects as Class I, flat spectrum, or II, place strong classification constraints on two objects, and more loosely restrict the classification of eight more objects. These observations will aid in interpretation of planned *SIRTF* observations of this cluster.

Key words: open clusters and associations: individual (NGC 1333) — stars: formation — stars: pre–main-sequence

1. INTRODUCTION

Since NGC 1333, part of the Perseus OB2 molecular cloud complex, is one of the nearest star-forming clusters, it is relatively well studied. Early NGC 1333 surveys include a *JHKL* study (Strom, Vrba, & Strom 1976, hereafter SVS), which resolved 25 sources, and the *IRAS* survey (Jennings et al. 1987), which found nine peaks. More recent higher resolution higher sensitivity surveys found 134 objects in broadband *JHK* (Aspin et al. 1994, hereafter ASR), 33 in the submillimeter continuum (850 and 450 μm; Sandell & Knee 2001, hereafter SK), and 44 in the radio continuum (6 and 3.6 cm; Rodriguez, Anglada, & Curiel 1999, hereafter RAC). From these surveys, one can identify several dozen candidate embedded objects in NGC 1333.

Lada & Wilking (1984) defined three classes of embedded young stellar objects (YSOs) based on the spectral index between the near- and mid-IR, 2 μm (K) to 10 μm (N). Class I objects have the largest spectral indices; Class II and III are thought to continue in a progressively less embedded (perhaps evolutionary) sequence toward the zero-age main sequence. (Wilking et al. (2001) redefined the boundaries of the classification scheme to include presumably transitional "flat spectrum" objects between Class I and Class II objects.) In 1993, "Class 0" was defined to encompass the earliest or most embedded stage of a young stellar object's lifetime (André, Ward-Thompson, & Barsony 1993). Some 42 (and counting) Class 0 objects are now known (André, Ward-Thompson, & Barsony 2000) from observations of a variety of star-forming regions. Four Class 0 objects, 10% of those known (André et al. 2000), are in NGC 1333, confirming its status as a young active region of star formation. NGC 1333 is also rich in young stellar outflows, with 36 cataloged Herbig-Haro objects[4] (Bally, Devine, & Reipurth 1996; Bally & Reipurth 2001), suggesting that many of the cluster members are actively accreting from circumstellar disks.

This Class 0–III (plus flat spectrum) classification scheme attempts to characterize the spectral energy distribution (SED) for an object via a single number. Alternate methods of summarizing the SED information in a single number are often useful; in some cases, detecting the object at K or N is not possible, so other parameterizations are necessary. One commonly used number is a temperature thought to be representative of the SED, and there are several methods to derive such a temperature. The most straightforward is a simple single-blackbody fit. For those objects detected only in *JHK*, we presumably have information on only the Wien side of the SED; a measurement at N will allow classification and, by adding data on the Rayleigh-Jeans side, help define the SED. Similarly, for those sources detected only in the millimeter or radio, presumably out on the Rayleigh-Jeans tail, a measurement at N may help define the SED by adding a point to the Wien side of the curve.

In theory *IRAS* observations combined with *JHK* data could allow the classification of deeply embedded sources. However, in addition to sampling wavelengths longer than those defining YSO classifications, the *IRAS* beams are huge compared with the source density in NGC 1333, and therefore source confusion is rampant. In every long-wavelength study after the original Jennings et al. (1987) *IRAS* paper, the nine original *IRAS* peaks have been split into more and more components; for example, as recently as 2001, SK discovered a third component in IRAS 2. So the *JHK* plus *IRAS* data are not sufficient to identify and characterize the young stellar objects in NGC 1333.

The existing near-IR, submillimeter, and radio surveys of NGC 1333 also all have resolutions $\gtrsim 3''$–$4''$; to cover a large area, the VLA was specifically used at a relatively low

[1] *SIRTF* Science Center, 220-6, California Institute of Technology, 1200 East California Boulevard, Pasadena, CA 91125; luisa.rebull@jpl.nasa.gov.

[2] Some of this work was carried out as a National Research Council Resident Research Associate, Jet Propulsion Laboratory, California Institute of Technology, 4800 Oak Grove Drive, Pasadena, CA 91109.

[3] Jet Propulsion Laboratory, 4800 Oak Grove Drive, Pasadena, CA 91109.

[4] See http://casa.colorado.edu/hhcat/.

resolution (RAC). Recently, a number of YSOs with luminous infrared companions have been found (e.g., the ρ Oph source WL 20; see Ressler & Barsony 2001; Wilking et al. 2001); it seems likely that others may be lurking in NGC 1333.

The resolution obtainable with the Jet Propulsion Laboratory (JPL) mid-IR camera MIRLIN at Palomar or at the NASA Infrared Telescope Facility (IRTF), $\sim 0\farcs5$, is significantly better than the existing long-wavelength surveys of NGC 1333, allowing us to resolve potential multiples in addition to classifying objects as Class I–III (or flat spectrum). In this paper, we discuss the 22 objects we observed with MIRLIN at Palomar Observatory and IRTF, combining our data with data from the literature to construct SEDs for each object.

SIRTF, due to be launched in 2003, will have wavelength coverage from 3.6 to 160 μm, with spatial resolution from $\sim 1\farcs5$ to $\sim 15''$. The MIRLIN observations are a nice complement to the planned *SIRTF* observations of NGC 1333; *SIRTF* can more easily cover the whole cluster than MIRLIN and achieve much higher sensitivity, but given *SIRTF*'s spatial resolution, information on individual source multiplicity obtained with a higher spatial resolution instrument (such as MIRLIN) can be used to better interpret *SIRTF* results.

2. OBSERVATIONS AND ANALYSIS

Using NASA's Astrophysics Data System, we combed the existing literature to find observations of sources in NGC 1333 and construct a target list. Our final target list is summarized with commonly used synonyms in Table 1. Data from the literature are summarized in Table 2. We observed primarily in *N* band; final new mid-IR flux values and limits are in Table 3.

2.1. *Literature Values*

The ASR *JHK* survey found 134 objects, 55 of which they concluded were likely pre–main-sequence objects. Lada, Alves, & Lada (1996, hereafter LAL) also conducted a *JHK* survey over a wider region, finding 143 sources they thought were associated with NGC 1333. The LAL source list of 130 objects detected in *J*, *H*, and *K* was obtained from C. Lada (2000, private communication), and the ASR and LAL catalogs were merged. In a color-magnitude diagram ($J-H$ vs. $H-K$), $\sim$20 unique objects are red enough to suggest that they are deeply embedded and therefore are candidate protostellar objects. One is a known Class 0 object, SVS 13=ASR 1 (André et al. 2000). Since 10 μm (*N* band) observations have the advantage of at least 5 times greater penetration through dust than 2 μm observations (though with a shallower flux detection limit), we hoped to detect at *N* most of these embedded objects seen at *JHK*.

The RAC VLA survey found 22 objects they identified as potential YSOs, based on the 3.6–6 cm spectral index, of which few were then associated with any known objects. SK conducted a submillimeter (450 and 850 μm) survey, detecting 33 objects, 22 of which they associated with known sources, some from RAC; many of these were multiple sources for which only single sources had been known. By combining the lists of objects that RAC and SK identified specifically as potential YSOs (rather than just density peaks), we find that 38 likely YSOs have never been detected shortward of 450 μm (with only submillimeter detections for 19). The available data make it likely that these objects are YSOs, but their SEDs are poorly determined because all the known points are on the Rayleigh-Jeans tail of the blackbody curve (we note that the centimeter radiation is actually not thought to be thermal dust emission but rather originates from free-free emission). It is not surprising that deeply embedded

TABLE 1
SYNONYMS FOR TARGETS DISCUSSED HERE

ID Used Here	ASR	SVS	LAL	HH[a]	IRAS[b]	SK	VLA[c]	Other
ASR 31	31	...	...	6	7	...	...	
ASR 32	32	...	...	6	7	...	...	
ASR 33	33	...	...	...	7SM1	21	27	
ASR 60	60	...	...	6	7	...	...	
ASR 77	77	...	...	...	...	...	...	
ASR 107a and ASR b	107	...	141	...	...	...	...	Getman et al. No. 28
ASR 108	108	...	141	...	...	...	...	
ASR 111	111	17	97	...	...	...	...	Getman et al. No. 16
ASR 112	112	5	300	17	...	...	...	Getman et al. No. 86
IRAS 2a	...	...	...	...	2a	8	7	
IRAS 2c	...	...	...	...	2c	9	...	
IRAS 4a	...	...	...	...	4a	4	25	
IRAS 4b	...	...	...	...	4b[d]	3	28	
IRAS 4c	...	...	...	...	4c	5	29	
IRAS 5	...	...	...	...	5	19	...	
IRAS 7SM2	...	...	...	...	7SM2	20	...	
SK 26	...	...	...	...	...	26		
SVS 12	114	12	181	...	6	...	43?	Near VLA 42 as well
SVS 15	118	15	154	...	...	...	8:	Getman et al. No. 32
SVS 16e and SVS 16w	106	16	171	...	...	...	...	X11, Getman et al. No. 39

[a] HH nomenclature; see http://casa.colorado.edu/hhcat/.
[b] IRAS nomenclature originates from Jennings et al. 1987.
[c] VLA nomenclature originates from RAC.
[d] Choi 2001 notes that IRAS 4BI/4BII were referred to as IRAS 4B/4C by Looney et al. 2000.

TABLE 2

OBSERVATIONS FROM THE LITERATURE

Source	R (mag)	I (mag)	i' (mag)	J (mag)	H (mag)	K (mag)	L (mag)	M (mag)	Q (mag)	50 μm (Jy)	100 μm (Jy)	350 μm (Jy)
ASR 31	21.3	...	>20.0	>18.6	>16.9	15.51	...	...	...	<55	<107	...
ASR 32	>21.5	...	>20.0	17.85	>16.9	15.03	...	...	...	<55	<107	...
ASR 33	>21.5	...	>20.0	17.23	16.70	15.07	...	...	...	<55	<107	...
ASR 60	19.8	...	17.5	16.56	16.38	14.25	...	...	...	<55	<107	...
ASR 77	>21.5	...	>20.0	17.28	14.88	13.33	...	...	...	...	...	...
ASR 107a and ASR b	19.7	...	17.4	13.62	12.00	10.52	9.20	...	...	...	...	...
ASR 108	17.7	...	15.9	12.72	11.33	10.00	9.39	...	...	...	...	...
ASR 111	>21.5	16.3	>20.0	12.81	11.69	10.76	...	...	...	...	...	...
ASR 112	>21.5	18.9	>20.0	14.28	11.69	10.31	...	...	...	...	...	...
IRAS 2a	...	...	...	...	...	...	...	...	...	<49	<67	<37.2
IRAS 2c	...	...	...	...	...	...	...	...	...	<49	<67	<37.2
IRAS 4a	...	...	...	...	...	...	...	...	...	<30	<143	71.0
IRAS 4b	...	...	...	...	...	...	...	...	...	<30	<143	51.7
IRAS 4c	...	...	...	...	...	...	...	...	...	<30	<143	...
IRAS 5	...	...	...	...	...	...	...	...	...	2	<26	...
IRAS 7SM2	...	...	...	...	...	...	...	...	...	<55	<107	...
SK 26	...	...	...	...	...	...	...	...	...	...	...	...
SVS 12	>21.5	...	>20.0	14.85	12.66	10.61	...	...	1.05:	<62	<204	...
SVS 15	18.2	17.9	16.0	11.51	9.90	9.90	7.80	...	...	...	...	...
SVS 16e	>21.5	...	>20.0	17.17	13.56	11.37	9.55	9.04	...	...	...	<6.1
SVS 16w	>21.5	...	>20.0	16.38	12.91	10.85	9.23	8.65	...	...	...	<6.1

Source	450 μm (Jy)	750 μm (Jy)	800 μm (Jy)	850 μm (Jy)	1.1 mm (Jy)	1.3 mm (Jy)	2.0 mm (Jy)	2.7 mm (Jy)	3.4 mm (Jy)	3.6 cm (mJy)	6 cm (mJy)
ASR 31	...	...	...	...	...	<0.54	...	...	...	...	...
ASR 32	...	...	...	...	...	<0.54	...	...	...	...	...
ASR 33	5.45	...	...	0.93	...	<0.54	...	...	...	0.83	0.48
ASR 60	...	...	...	...	...	<0.54	...	...	...	...	...
ASR 77	...	...	...	...	...	...	...	...	...	...	...
ASR 107a and ASR 107b	...	...	...	...	...	...	...	...	...	...	...
ASR 108	...	...	...	...	...	...	...	...	...	...	...
ASR 111	...	...	...	...	...	...	...	...	...	...	...
ASR 112	...	...	...	...	...	...	...	...	...	...	...
IRAS 2a	23.7	<5.54	<3.75	3.27	<1.46	<0.875	<0.32	0.0224	...	0.25	0.06
IRAS 2c	2.38	<5.54	<3.75	0.37	<1.46	<0.875	<0.32	...	...	...	...
IRAS 4a	29.7	...	12.9	9.05	6.27	4.10	1.75	0.604	0.303	0.49	0.36
IRAS 4b	22.72	...	8.55	4.64	3.64	1.5	0.76	0.314	0.144	<0.10	0.07
IRAS 4c	3.95	...	...	0.93	...	...	...	...	...	<0.11	0.08
IRAS 5	3.70	...	...	0.29	...	...	...	...	...	...	...
IRAS 7SM2	3.58	...	...	0.58	...	<0.54	...	...	...	...	...
SK 26	38.0	...	...	5.42	...	...	...	...	...	...	...
SVS 12	...	...	...	...	...	...	...	<0.012	...	...	0.16:
SVS 15	...	...	...	...	...	...	...	...	...	0.04:	<0.04:
SVS 16e	...	...	<0.2	...	...	<0.057	...	...	...	...	...
SVS 16w	...	...	<0.2	...	...	<0.057	...	...	...	...	...

TABLE 3
NEW MID-IR OBSERVATIONS

Source	Flux at N[a] (Jy)	Flux at $N5$[b] (Jy)	Flux at Qs[b] (Jy)	Flux at $Q5$[b] (Jy)
ASR 31	<0.023	...	...	...
ASR 32	<0.023	...	...	...
ASR 33	<0.023	...	...	...
ASR 60	<0.027	...	...	...
ASR 77	<0.056	...	...	...
ASR 107a	0.076 ± 0.001	...	...	...
ASR 107b	~0.02	...	...	...
ASR 108	0.021 ± 0.01	...	...	...
ASR 111	<0.055	...	...	...
ASR 112	0.167 ± 0.002	...	...	...
IRAS 2a	<0.020	0.314 ± 0.03	0.735 ± 0.08	8.85 ± 0.9
IRAS 2c	<0.034	...	...	...
IRAS 4a	<0.023	...	...	<0.921
IRAS 4b	<0.020	...	...	...
IRAS 4c	<0.023	...	...	...
IRAS 5	<0.029	...	...	...
IRAS 7SM2	<0.036	...	...	...
SK 26	<0.024	...	...	...
SVS 12	1.38 ± 0.006	...	4.72 ± 0.1	6.53 ± 0.7
SVS 15	<0.038	...	...	...
SVS 16e	0.087 ± 0.001	...	<0.644	...
SVS 16w	0.130 ± 0.001	...	<0.644	...

[a] Data from Palomar; the central wavelength is 10.79 μm, with a passband width of 5.66 μm.
[b] Data from IRTF; $N5$, Qs, and $Q5$ filters have central wavelengths 12.49, 17.90, and 24.48 μm and passband widths 1.16, 2.00, and 0.76 μm, respectively.

sources visible in the submillimeter (or radio) do not have *JHK* counterparts, but again, given that mid-IR observations can see deeper into the dust than 2 μm, we expected to detect some embedded stellar cores found in longer wavelengths but missed in *JHK*.

After merging these catalogs of likely embedded objects, we compared the resulting target list with the Catalog of Herbig Haro Objects[5] to ensure that we were looking at YSOs, not shocked ejected material. We omitted SVS 13 from the present study because it will be discussed by Cole et al. (2003). We also omitted some objects (such as IRAS 2b) because a sufficiently optically bright guide star was not available. Our final observed target list consisted of 19 pointings (21 previously known objects). Ten of these had previous detections only in short wavelengths (largely *JHK*, with a few *LM*), and eight had detections only in long wavelengths ($\geq$450 μm). Three had detections at both short and long wavelengths (although some of the long-wavelength source matches were tentative). Our final target list is intentionally biased toward finding the most embedded objects. We used coordinates from ASR whenever possible; otherwise we used those from SK.

Other surveys we consulted for supporting data on these sources include the following: Preibisch, Neuhauser, & Stanke (1998; X-rays and *JHKLM*), Getman et al. (2002; X-rays and Sloan *i'*), SVS (*JHKL*), Harvey, Wilking, & Joy (1984; *JHKLM*), Aspin & Sandell (1997; *L*), Molinari, Liseau, & Lorenzetti (1993; *Q*), Jennings et al. (1987; *IRAS* 50 and 100 μm), Cohen & Schwartz (1987; *IRAS* 12, 25, and 60 μm), Lay, Carlstrom, & Hills (1995; 0.84 mm), Sandell et al. (1994; 2, 1.3, and 1.1 mm and 800, 750, 450, and 350 μm), Sandell et al. (1991; 2, 1.3, and 1.1 mm and 800, 450, and 350 μm), Smith et al. (2000; 850 and 450 μm), Lefloch et al. (1998; 1.25 mm), Motte & André (2001; 1.3 mm), Looney, Mundy, & Welch (2000; 2.7 mm), and Choi (2001; 2.7 and 3.4 mm). In general, more recent measurements were preferred over older measurements at the same wavelength.

Since we are combining data from multiple surveys and using them to construct SEDs of (presumably) individual objects, the resolution of each survey can be a factor. If there are unresolved nearby companions for any of these objects, the flux values associated with one object may actually be generated by two (or more) objects. Since each of the objects observed here (except for ASR 107; see below) is thought to be single, based on the best observations to date, for the most part we accepted at face value the total flux (not surface brightness) reported in the literature as associated with the objects listed. In cases in which the literature values were obtained with substantially poorer spatial resolution (e.g., Jennings et al. *IRAS* survey and SVS, ~30″ resolution), the detections were treated as unapportioned upper limits for the object being considered. The near-IR surveys generally have high spatial resolution at ~1″–3″. Essentially all the 450 μm data have ~8″ resolution, and the 850 μm data, ~14″. The millimeter and centimeter data are ~4″–5″. The risk of including flux from an unseen companion is greatest for the 850 μm data. However, all objects considered here are detected and thought to be single at other wavelengths. For the 12 objects with near-IR detections, there are no previously known companions at separations greater than 1″–3″. For the eight objects with only longer

[5] See http://casa.colorado.edu/hhcat/.

wavelength detections, there are no previously known companions at separations greater than $\sim 4''$–$5''$.

Aspin (2003) and Preibisch et al. (1998) show that state-of-the-art instrumentation on large ground-based telescopes is capable of obtaining near-infrared spectra that provide approximate spectral types for embedded sources in NGC 1333 and other regions. If a temperature can be inferred from the spectral type, the observed photometric spectral energy distribution may be fitted by a reddened stellar photosphere, as is done for a few of the sources in this paper. Departures from this type of fit may indicate varying grain properties (unusual extinction laws) in the molecular cloud environment or excess emission due to circumstellar material. As more such spectroscopic data become available, they will greatly enhance the value of photometric measurements such as those reported here.

2.2. *New Observations*

2.2.1. *MIRLIN Mid-IR Data*

Observations were conducted on the nights of 2001 September 28 and 29 on the Palomar 5 m ($200''$) telescope by using the JPL mid-IR camera MIRLIN (mid-infrared large-well imager). MIRLIN is a 128×128 pixel 7–25 μm infrared astronomical camera built at JPL by a team led by Michael Ressler (Ressler et al. 1994). At Palomar, MIRLIN has a pixel scale of $\sim 0\farcs15$ pixel^{-1} ($19''$ field of view), and of the available filter suite broadband N is the most effective. The central wavelength of the N filter is 10.79 μm, with a passband width of 5.66 μm. Data were taken using a three-beam chop-nod pattern with a chop throw and nod distance selected to place all three beams on the array, e.g., the beams appear in a diagonal pattern: $4\farcs5$ north and west of the center, the center, and $4\farcs5$ east and south. Each frame was examined to be sure that no other sources appeared.

Additional observations were conducted during engineering time using MIRLIN at the NASA 3 m IRTF on Mauna Kea during the nights of 2001 October 22–24. At this telescope, MIRLIN has a pixel scale of $\sim 0\farcs475$ pixel^{-1} ($61''$ field of view). Broadband N generally cannot be used with MIRLIN at the IRTF because the array saturates too quickly; we used $N5$, Qs, and $Q5$ filters instead, which have central wavelengths 12.49, 17.90, and 24.48 μm, and passband widths 1.16, 2.00, and 0.76 μm, respectively. Chopping and nodding were performed as at Palomar, except with an amplitude of $\sim 14''$.

In both cases, standards were observed interspersed with the targets. Data were processed using our in-house IDL routine MAC (match and combine), originally developed specifically for use with MIRLIN data by K. A. Marsh and updated by various collaborators. Circular aperture photometry was performed on both the targets and the standards taken throughout the night by using an aperture of radius 5 pixels. In the case of SVS 16, the binary components were too close together for a 5 pixel aperture, so we used 3 pixels (reprocessing the relevant standards). For computing upper limits, we allowed MAC to select and combine peaks in the noise for a worst-case conservative limit. Final flux values and 3 σ limits are in Table 3.

2.2.2. *OVRO and CSO Data*

Additional data for SVS 12 (detections and limits) and SVS 16 (upper limits) come from both the Owens Valley Radio Observatory (OVRO) and the Caltech Submillimeter Observatory (CSO). The OVRO observations were taken in the fall of 1989 by using four configurations of three 10.4 m telescopes. The synthesized beam was $9\farcs0 \times 6\farcs7$ at a position angle of 0°. The 110 GHz continuum was observed in a 375 MHz wide channel, and the 3 σ continuum sensitivity was 12 mJy; however, SVS 12 was not detected. (SVS 16 was not observed.)

The CSO bolometer observations were made on 1990 December 11 and 14. The CSO beam size was $27''$ at 1.1 mm, $19''$ at 0.79 mm, and $15''$ at 0.63 mm. The optical depth at 225 GHz was 0.05–0.08 during the observations. Mars was used as a pointing and flux calibrator. Twenty pairs of ON/OFF source measurements were made with a $200''$ chop throw, which were then medianed to produce the final flux densities. At the CSO, SVS 12 is strongly detected with the following flux densities: 0.68 ± 0.03 Jy at 1.1 mm, 0.92 ± 0.07 Jy at 0.79 mm, and 3.07 ± 0.40 Jy at 0.63 mm. SVS 16 was not detected at 800 μm to a 3 σ limit of 200 mJy.

2.3. *Basic Analysis*

For each object, we fitted via χ^2 minimization a simple blackbody (BB) to the available detections at all wavelengths. Final best-fit values for the BB temperature T appear in Table 4. In cases for which the literature values were obtained with substantially poorer spatial resolution (e.g., *IRAS*), the detections were treated as unapportioned upper limits for the object being considered.

In most cases, we have only a few detections per object, and those few detections are not necessarily at the longest wavelengths. In general, the sources are not resolved. Thus, fitting anything more complicated than a simple blackbody is not merited. In cases in which we have a spectral type (e.g., SVS 16e and SVS 16w) we attempted to fit a reddened BB. In those cases with detections over a broad range of temperatures we attempted to fit a modified blackbody, which includes the optical depth at long wavelengths.[6] However, none of these fits were improvements on the initial BB fits. Although in reality all these sources are undoubtedly more complicated than simple blackbodies, in an attempt to place these sources in context with other similar objects we estimated the luminosity implied by the BB fit; see Table 4. The distance to NGC 1333 is uncertain; Cernis (1990) obtains a distance of 220 pc, whereas de Zeeuw et al. (1999) obtain 318 pc. We assumed a distance of 220 pc to ensure conservative lower limits on luminosities; assuming a distance of 318 pc increases all the luminosities by about a factor of 2. We note that a BB fit is appropriate only for thermal radiation, and the centimeter emission is thought instead to be free-free radiation. In only one case did the inclusion or omission of the centimeter point significantly alter the blackbody fit; see discussion below.

The 2 μm (K) to 10 μm (N) slope of each SED is of interest for classifying these objects. For those objects with K and N detections, we can explicitly calculate the slope; for other objects with upper limits in N, we can constrain the classification of each object. Following Wilking et al. (2001), we define the spectral index as $a = d\log \lambda F_\lambda / d\log \lambda$, where $a > 0.3$ for a Class I, 0.3 to -0.3 for a flat-spectrum source, -0.3 to -1.6 for a Class II, and less than -1.6 for a Class III. Final slopes and classifications appear in Table 4.

[6] A modified blackbody is given by $F_\lambda = \Omega B_\lambda T(1 - e^{-\tau})$, where $\tau = (\lambda_0/\lambda)^\beta$, Ω is the angular size of the object, and β is fixed at 1.5.

TABLE 4
Blackbody Best-Fit Temperature and SED Classifications

Source	BB Temp.[a] (K)	L^b ($L_\odot$)	2–10 μm Spectral Index	Class
ASR 31	2050	0.001	<1.5	
ASR 32	1550	0.002	<1.3	
ASR 33	400[c]	...	<1.3	
ASR 60	2400	0.003	<0.9	
ASR 77	1100	0.01	<0.8	
ASR 107a	1450	0.1	−0.6	II
ASR 108	1850	0.1	−1.3	II
ASR 111	1800	0.1	< −0.7	II–III
ASR 112	1100	0.4	−0.2	Flat spectrum
IRAS 2a	100	3.	Large?	0?[d]
IRAS 2c	<50	0.1	Large?	[d]
IRAS 4a	<50	2.	Large?	[d]
IRAS 4b	<50	1.	Large?	[d]
IRAS 4c	<50	0.2	Large?	
IRAS 5	50	0.5	Large?	
IRAS 7SM2	<50	0.2	Large?	
SK 26	<50	2.	Large?	
SVS 12	550[e]	24	1.3	I
SVS 15	1450[f]	0.4	< −1.4	II–III
SVS 16e	850	0.1	−0.03	Flat spectrum
SVS 16w	900	0.2	−0.08	Flat spectrum

[a] Blackbody best-fit temperature.
[b] Luminosities implied by the fits using 220 pc distance; using a distance of 318 pc increases all the luminosities by about a factor of 2. To adjust for another distance (d) in parsecs multiply by $(d/220\ \mathrm{pc})^2$.
[c] The best-fit single-blackbody temperature for this object, at 1950 and 50 K. The corresponding luminosities are 0.001 and 1.6 $L_\odot$, respectively, for each of the components.
[d] André et al. 2000 cite IRAS 2 (aggregate), IRAS 4a, and IRAS 4b as genuine Class 0 objects.
[e] The best-fit single-blackbody temperature for this object is 550 K. However, this object may be better fitted by two blackbodies, at 1100 and 150 K.
[f] For the fit that includes the tentative match with a VLA object, the best-fit temperature is 1100 K (and the luminosity is 4 $L_\odot$ at 200 pc).

3. DISCUSSION OF INDIVIDUAL OBJECTS

3.1. *ASR 107 and ASR 108*

We detected three objects in a field of view where ASR saw two objects (ASR 107 and ASR 108) and LAL only one. Identifying the brightest object we detect as ASR 107, a faint object appears at a net distance of 0.″74 and at position angle 324°. A second, more distant object (presumably ASR 108) is at a net distance of 3.″81 and position angle 166°.

3.1.1. *MIRLIN Data*

The MIRLIN data have a much higher spatial resolution (∼0.″50) than either LAL or ASR, and we expected to be able to resolve ASR 107/108, provided we could detect them. Since ASR 107 and 108 are each detected in *RIJHKL*, a blackbody fit suggests that it is likely that they can be detected at *N*.

We dithered over a region ±6″ north and south of the nominal ASR 107 position looking for other objects; all the sources we detected appear in the final MIRLIN image in Figure 1, with fluxes for every source in Table 3. In addition to a prominent bright object, two low-level but clearly detected sources appear. These objects are very faint, but their presence is repeatable in subsets of the data (and in the positive and negative beams) and are therefore real.

3.1.2. *Previous Detections*

The reported spatial resolution of LAL is 1.″36, so in theory LAL could resolve this pair. However, only one object appears in this field in the LAL catalog. The listed magnitudes for the LAL object are comparable to the magnitudes listed for ASR 108; the difference in magnitudes are 0.13 mag in *J*, 0.07 mag in *H*, and 0.44 mag in *K*. Young stars are known to be variable in *JHK* to at least this amplitude (e.g., Carpenter, Hillenbrand, & Skrutskie 2001; Carpenter et al. 2002), so variations of this order are not surprising.

ASR describe ASR 108 as being 0.″29 east and 1.″8 south of ASR 107. The net separation of 1.″82 is slightly larger than the stated ASR spatial resolution of 1.″24. This reported separation between ASR 107 and 108 is in the same direction as the separation of our two brightest objects but is about half our observed separation.

Aspin & Sandell (1997) discuss these objects, and Aspin (2003) discusses ASR 107 but not 108; neither notes any irregularities in the coordinates. There are no other detections of these objects discussed in the literature. However, J. Bally has recently made public the Hα images of NGC 1333 from Bally et al. (1997) and Bally & Reipurth (2001). These observations have a pixel scale of 0.″68 pixel^{-1} and 0.″26 pixel^{-1}, respectively, and as such can easily resolve ASR 107/108. Both these images reveal a pair of clearly detected

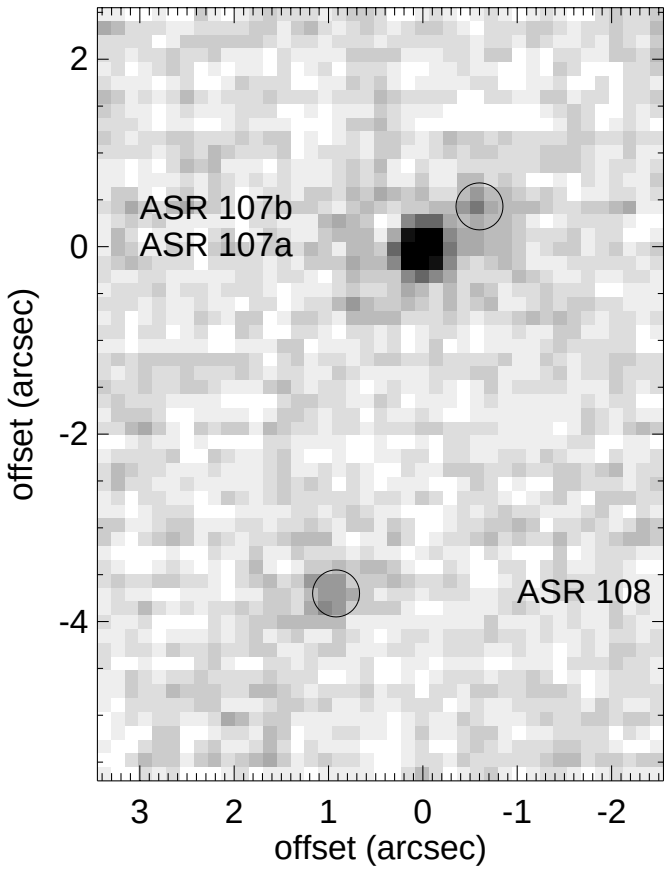

FIG. 1.—MIRLIN images of sources near ASR 107. North is up, and east is left. The brightest object is ASR 107a, the faint object to the northwest is a new object (ASR 107b), and the faint object to the southeast is ASR 108. These objects are very faint, but they are repeatable in subsets of the data (and in the positive and negative beams) and are therefore real.

stars, with a separation nearly identical to the separation of the two brighter stars in the MIRLIN data, in contradiction to the separation reported in ASR. No counterpart to our faint northwest object is apparent in these data, but the spatial resolution is such that none is expected.

3.1.3. *Uncertainties and Implications*

Because these objects are undetected in the optical and the MIRLIN field of view is too small to include other astrometric reference objects, we cannot know the absolute astrometry of any of the objects we detected. This makes optical associations with our *N*-band detections difficult. However, since ASR 107 and 108 are each detected in *RIJHKL*, we expected (based on simple blackbody fits) to be able to detect both objects in *N*. Since there are no other detected objects within several arcseconds, since the relative orientation of the two objects we detected is the same as those for ASR 107/108, and since the Bally images support our observed separation, we conclude that it is most likely that the bright northern object is ASR 107 and the southern object is ASR 108. C. Aspin (2002, private communication) confirms that it is likely that the astrometry reported in ASR is incorrect (perhaps an artifact of the combination of many small images to obtain the final mosaic) and that we have correctly identified our two 10 μm sources with ASR 107 and ASR 108.

3.1.4. *SEDs and Classifications*

We proceed on the assumption that the bright object is ASR 107a (with the faint northwest object being ASR 107b) and the faint southern object is ASR 108; we used those data accordingly for the SEDs in Figure 2. With only one point for ASR 107b, we were obviously unable to construct an SED. For both ASR 107a and 108, the only detections are at *N* and shorter wavelengths, but turnover in the SED can be clearly seen. ASR 107a suggests a 1450 K BB fit; ASR 108, though having a fainter *N* flux, is slightly warmer at 1850 K. The fits imply luminosities of $\sim$0.1 $L_\odot$ for both objects. ASR 107a has a 2–10 μm slope of -0.6, and ASR 108 has a slope of -1.3, placing them both in Class II.

Aspin (2003) discusses ASR 107, assigning it a blackbody temperature of $\sim$3000 K, warmer by about a factor of 2 than our fit suggests. Aspin also assigns a spectral type of K2 V based on 2 μm spectroscopy. Fits using these parameters and either a BB or a reddened BB produce worse fits than appear in our Figure 2 (which fits a plain BB).

3.2. *SVS 16e and SVS 16w*

SVS 16 (Fig. 3) was resolved into two components by Preibisch et al. (1998). They derive 12, 25, 60, and 100 μm flux limits from *IRAS*; these limits (along with our CSO limit at 800 μm) appear in Figure 2. Preibisch et al. were not able to detect these objects in *N* and so were unable to formally classify these objects as Class I, II, or III or flat spectrum (the latter of which didn't exist as a classification at that time); however, on the basis of IR spectroscopy, they argued that the objects are both Class II or III sources. They also classified SVS 16w as spectral type M2, and SVS 16e as M3. Aspin (2003) suggests that SVS 16 (aggregate) is an M0.

We detect both objects in *N* but not in *Qs*. We find that SVS 16w is brighter than SVS 16e in *N* by 50%; at shorter wavelengths, 16e is brighter. Using the same methodology as for the rest of the sources in this paper, we estimate that these two objects are very close to each other in blackbody temperature, $\sim$850 and $\sim$900 K. The luminosities implied by the BB fits are $\sim$0.1–0.2 $L_\odot$. Note that these fits are reported here for completeness and comparison with other objects in this work; because we have a spectral type for these objects, we have a much better estimate of the intrinsic temperature of each YSO and therefore can fit a reddened blackbody to the SED. We derive $A_v \sim 26$ and 23 for SVS 16e and SVS 16w, respectively. Based on these fits, our *N*-band fluxes are almost all excess; only 10% of the flux is due to the photosphere. The western component has 30% more excess than the eastern component.

Now that there are *N* detections, we can formally classify the objects by calculating the 2–10 μm slopes. The slopes we calculate for SVS 16e and SVS 16w are -0.03 and -0.08, respectively, suggesting both objects are flat-spectrum sources. This relatively new classification did not exist when Preibisch et al. (1998) estimated these objects as Class II or III on the basis of other observations.

3.3. *SVS 12*

3.3.1. *Previous Observations*

Even by the standards of NGC 1333, SVS 12 is a well-studied source. Two previous determinations of the bolometric luminosity of SVS 12 have been made: 28 $L_\odot$ (Jennings et al. 1987) and 13 $L_\odot$ (Cohen & Schwartz 1987).

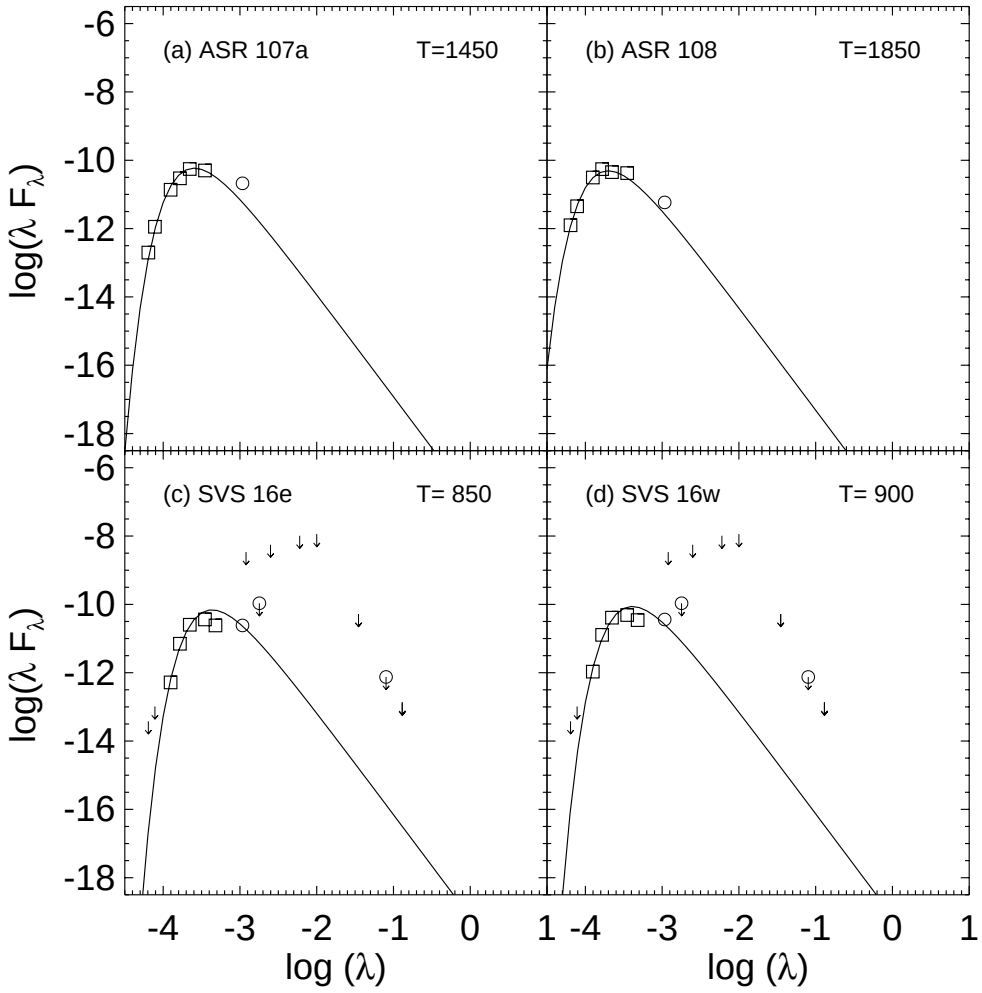

FIG. 2.—SEDs for sources with companions, showing detections from the literature (*squares*), upper limits (or unapportioned flux) from the literature (*arrows*), detections in *N* presented here (*circles*), upper limits in *N* or *Qs* (*circles with arrows*), and a simple BB fit (*line*); see text. λ and $\lambda F(\lambda)$ are in cgs units. Best-fit temperatures are included in each figure and are listed in Table 4.

Both values suggest that SVS 12 is a low-mass star ($<2M_{\odot}$). Previous temperature determinations for this object range from 37 K (Jennings et al. 1987) to 50–176 K (Cohen & Schwartz 1987). Near-infrared imaging indicates very strong circumstellar extinction (Stapelfeldt et al. 1991). For the star itself, $J-K \geq 6$ mag; however, an adjacent reflection nebula is substantially less reddened, with $J-K = 3$ mag.

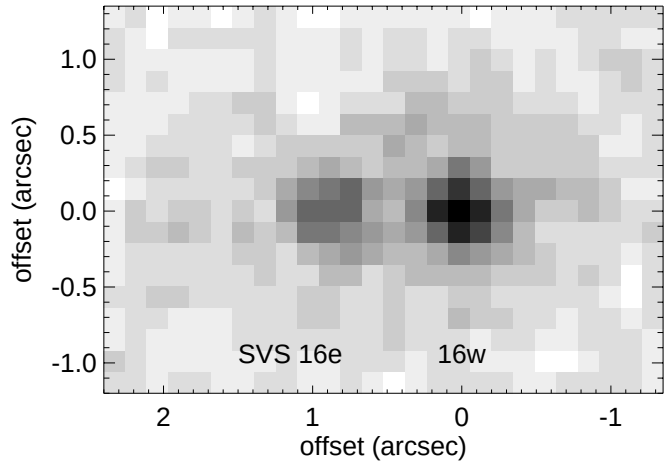

FIG. 3.—MIRLIN images of SVS 16e and SVS 16w. North is up, and east is left.

There are several objects thought to be possibly associated with SVS 12. Within a MIRLIN field of view centered on this object, there are four potentially different objects in the literature. Figure 4 plots the four objects by using coordinates from their respective discovery papers. We pointed nominally at ASR 114=SVS 12=IRAS 6=LAL 181. Based on the accuracy of their coordinates, which they claim are good to 0.″5, RAC do not think that VLA 42 and VLA 43 are associated with SVS 12; SVS 12 is 2″ away from VLA 43. On the other hand, SK say VLA 42 lies within 2.″5 of SK 24 and list those two as associated. The listed position for SK 24 is 7.″7 away from the SVS 12 position; it seems unlikely that SK 24 and SVS 12 are actually the same object. SVS 12 is closest to VLA 43, so if any of the VLA sources are truly associated with SVS 12, it would be this one. Despite the fact that the emission at centimeter wavelengths is not thought to be from thermal dust emission, we attempted SED fits (see below) for SVS 12 both with and without this detection associated with VLA 43. As this VLA point is consistent with the (blackbody) slope found from our CSO data for this object, inclusion or omission of this point had no effect on the fit.

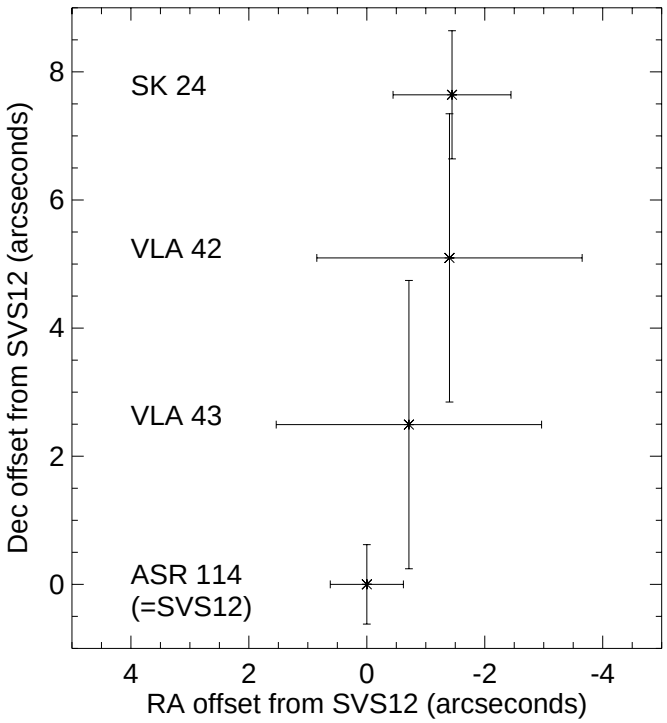

FIG. 4.—Objects near SVS 12 from the literature that are well within a MIRLIN field of view centered on SVS 12. The error bars on each point correspond roughly to spatial resolution, e.g., FWHM beam size, not reported coordinate uncertainties, which are generally less than the beam size.

3.3.2. *MIRLIN and CSO Data*

We detected SVS 12 in three CSO wavelengths (1.1, 0.79, and 0.63 mm) and in three mid-IR passbands, *N* at Palomar, and at *Qs*, and *Q5* at IRTF. In the *N* images, we apparently resolve SVS 12 into something larger than a point source. Figure 5 shows images of an average standard, SVS 12, and the residual left when subtracting the average standard from SVS 12; Figure 6 shows average radial profiles of same. The average standard was constructed using a weighted mean of seven images of three standards (β And, α Ari, and α Aur) taken immediately before and after the SVS 12 observation. The average standard and the object flux distributions were scaled to the same relative peak intensity before subtraction. Because the signal-to-noise ratio (S/N) of the average standard was at least 100 times that of SVS 12 (as is reflected in the errors associated with the pixels shown in Fig. 6), any extended features found in the point-spread function (PSF) of the average standard are scaled down for comparison with the fainter object.

It is apparent from both Figures 5 and 6 that the SVS 12 image has a wider PSF than the standards. The general asymmetric shape persists in subsets of the data, but the S/N of the subtle northwest extension seen in Figure 5 is too low to be evaluated in subsets of the data. If this extension is real, it is in the same direction as the extension of the nebula seen in *K*-band observations (Stapelfeldt et al. 1991; Stapelfeldt 1994).

SVS 12 does not appear to be extended in *Qs* or *Q*5. However, for the *Qs* data in particular seeing seemed to get worse during the observations of this particular object and the standards obtained near it.

3.3.3. *Interpretation*

From physical principles, the radius of the blackbody emission peak from a continuous optically thin dust disk or envelope will be $\propto\lambda^2$. Any thermal source would thus be expected to be $\sim$4 times more extended at *Q* than at *N*. However, in this case our *N* observations come from the 5 m telescope at Palomar and our *Q* from the 3 m IRTF, so the PSF size has also increased, but only by a factor of 3.3. Thus for data sets of equivalent S/N, a dusty source should still actually be better resolved (by a factor of about 1.2) at IRTF in *Q* band than at Palomar in *N* band. Since we are not seeing this, it argues against dust thermal emission for the extended *N*-band emission. We can also argue against thermal emission just from the physical scale of the extended emission ($\sim$0$''$.5 = 110 AU at 220 pc, 160 AU at 320 pc); to have dust at this distance at a temperature of 300 K, the central star luminosity would have to be greater than 7000 $L_\odot$ (from $L = 4\pi r^2\sigma T^4$). This luminosity would have been detected by *IRAS*, which measured only about 30 $L_\odot$ for this source (Jennings et al. 1987). Other stars known to be extended in the mid-IR are indeed highly luminous Herbig Ae stars (e.g., Marsh et al. 1995). So we conclude that it is unlikely that we have resolved thermal emission from the circumstellar material of SVS 12. One possibility is that we could be seeing reflected light at *N* band. Another possible interpretation is that SVS 12 is a close binary. Simple simulations suggest that a PSF similar to that we observe in *N* can be recovered via a binary with a separation of $\sim$0$''$.2. This separation would not be resolvable at the IRTF and only marginally resolvable at Palomar, consistent with our observations.

3.3.4. *SED and Classification*

Working on the assumption that this is a single object, we plot the SED for this source in Figure 7, including *IRAS* fluxes from Cohen & Schwartz (1987) at 12, 25, and 60 μm (but not at 100 μm). The 2–10 μm slope is 1.3, making it a Class I source.

The spectral shape is not well fitted by a single blackbody, a reddened blackbody, or a modified blackbody. We fitted the shorter wavelengths separately from the longer wavelengths with simple blackbodies in Figure 7*b*. The cluster of mid-IR points seems to have a positive slope as a function of wavelength; the fit with multiple blackbodies better reproduces this slope, another possible indication that it is actually a binary.

We derive a luminosity consistent with previous determinations, $\sim$25 $L_\odot$. The hotter blackbody component, at 1100 K, is much hotter than previous temperature estimates; the cooler blackbody component (150 K) is consistent with earlier estimates. The inclusion or omission of the tentative match with the VLA source discussed above does not affect the fits because of the slope suggested by the CSO points. Most recently, Aspin (2003) discusses the 2 μm spectrum of this object as being featureless except for H_2 emission. This object seems to be unusual or at least different than other objects found in this cluster in several ways.

3.4. *ASR 112*

We detected ASR 112 in *N*. Previously all detections of this object had been in wavelengths shorter than 10 μm; the *N* detection seems to suggest a rollover in the SED. Previously, ASR had guessed that this object was in the spectral type

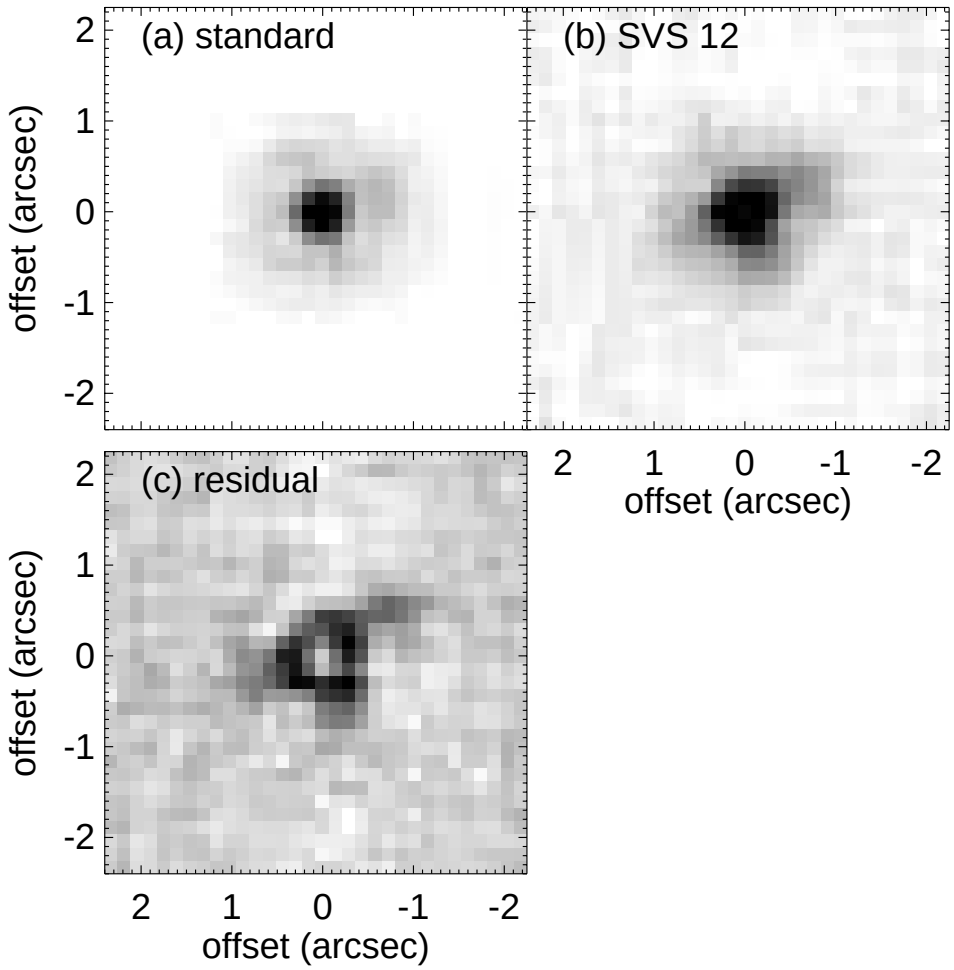

FIG. 5.—SVS 12 resolved in *N*: MIRLIN images of (*a*) average standard taken before and after data for SVS 12, (*b*) SVS 12, (*c*) residual left when subtracting the average standard from SVS 12. North is up, and east is to the left.

range K0–K3. Our best-fit BB is 1100 K. The total luminosity implied by the BB fit is $\sim$0.4 $L_{\odot}$. This object has a 2–10 μm slope of -0.2, making it a flat-spectrum object.

Aspin (2003) fits a BB at $\sim$1400 K, similar to our result. He confirms this object as early K, putting $T_{\rm eff} \sim 5080$ K, the intrinsic total luminosity (not the luminosity implied by the BB fit), at $\sim$5 $L_{\odot}$, the mass at $\sim$1 $M_{\odot}$, and the age at $\sim 10^6$ yr. Fitting a reddened 5080 K BB suggests that $A_v \sim 18$ and that this object has 10 times more flux at *N* than expected from the photosphere alone.

3.5. *IRAS 2a and IRAS 2c*

The objects associated with IRAS 2 have been well studied in multiple wavelengths. We observed IRAS 2a and IRAS 2c; neither was detectable from Palomar at *N*, but IRAS 2a was detected in *N*5, *Qs*, and *Q*5 from IRTF. Figure 8 presents the resulting SEDs. Recall that we have treated the *IRAS* detections as unapportioned upper limits because we have no way to accurately apportion the flux attributed to IRAS 2 among its constituent parts; thus, for any single component, the true contribution at *IRAS* wavelengths is necessarily less than the aggregate *IRAS* flux.

All the prior detections for the individual source IRAS 2a are on the long-wavelength, presumably Rayleigh-Jeans, side; our observations extend the SED to the Wien side for the first time. This is a cool object at $\sim$100 K whether or not the centimeter wavelength points are included in the fit. IRAS 2c has many fewer points, and the fit is relatively unconstrained. With only the existing long-wavelength detections, the temperature could be high. However, our upper limit in *N* constrains this object to be much cooler, $\lesssim$50 K. Based on 1.3 mm observations Motte & André (2001) report a bolometric temperature of 41 K for IRAS 2 (aggregate); our temperature estimates are consistent with that value.

Motte & André (2001) classify IRAS 2 as Class 0. In any case, these objects are deeply embedded.

3.6. *IRAS 4a, 4b, and 4c*

Unfortunately, we did not detect IRAS 4a, 4b, or 4c. Nonetheless, we have added our upper limits to the SEDs in Figure 8. Recall that we have treated the *IRAS* detections as unapportioned upper limits because we have no way to accurately apportion the flux attributed to IRAS 4 among its constituent parts. Thus, for any single component, the true contribution at *IRAS* wavelengths is necessarily less than the aggregate *IRAS* flux. A limit of 0.8 Jy for IRAS 4a at 0.84 mm from Lay et al. (1995) also appears in Figure 8*c*.

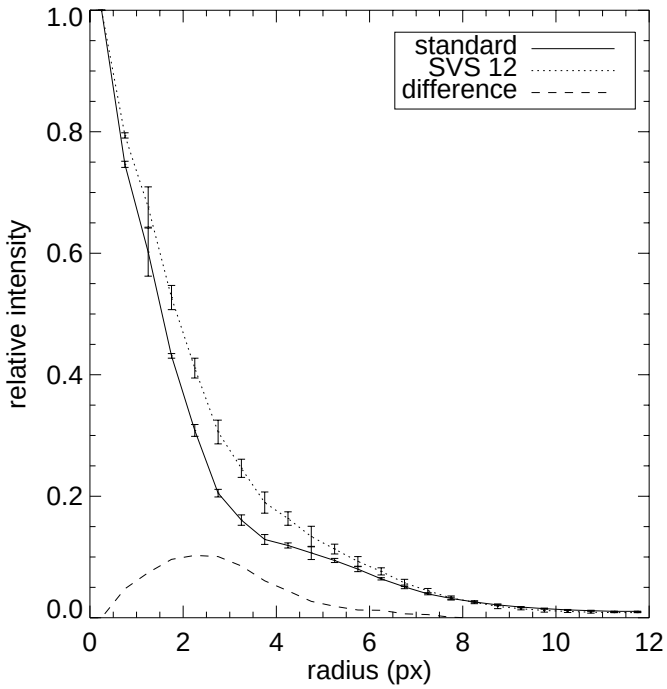

FIG. 6.—SVS 12 resolved in *N*: average radial profiles for SVS 12, the average standard near the SVS 12 data, and the residual left when subtracting the standard from the SVS 12 data.

In each case, the BB fit suggests that these objects are quite cool, $\lesssim$50 K, whether or not the centimeter wavelength points (thought not to arise from dusty thermal emission) are included in the fit.

Motte & André (2001) report bolometric temperatures of 34 and 36 K, respectively, for IRAS 4a and IRAS 4b; Jennings et al. (1987) estimate a temperature of 33 K. Our $\lesssim$50 K values are consistent with these temperatures.

Motte & André (2001) classify IRAS 4a and 4b as Class 0. In any case, these objects are deeply embedded.

3.7. *IRAS 7 Components: ASR 31, 32, 33, and 60, and IRAS 7SM2*

Several sources are listed in the literature as contributing to the total flux of IRAS 7; four sources are detected in *JHK* (ASR 31, 32, 33, and 60) and one only in the submillimeter (IRAS 7 SM2; see Knee & Sandell 2000). We needed three MIRLIN pointings to cover these objects. ASR 31, 32, and 33 all appear in the same field of view, but ASR 33 was thought to be the best target for *N*-band observations because it is detected at *JHK* and several other longer wavelengths. However, we did not detect any of these objects. SEDs with existing detections and upper limits appear in Figure 9.

ASR 31, 32, and 60 are measured on only one side of the SED, presumably the Wien side of the curve. The BB best-fit temperatures are ~2050, ~1550, and ~2400 K, respectively. For IRAS 7SM2, there are only a few detections, all on the long-wavelength side of the curve. Our detection limit at *N* constrains the temperature of this object to be rather low, $\lesssim$50 K; without our upper limit, this object could be high, based just on the slope of the two measured points.

It is unexpected that we did not detect ASR 33, given the measured fluxes. A single BB fit ($T = 400$ K) suggests that this object should have been easily detected at *N*. However, a two-blackbody fit could explain our nondetection at *N*; see Figure 9*f*, where the temperatures of these two blackbodies are 1950 and 50 K. The corresponding luminosities implied by these fits are 0.001 and 1.6 $L_\odot$, respectively, for the components. We suspect that we are seeing a highly reddened photosphere and reradiation by the surrounding dust.

It is possible that the reason we did not detect this object is that the detections have not been accurately matched across wavelengths to the same source or that observations with poorer spatial resolution are detecting flux from more than one object. SK identify SK 21 with IRAS 7SM1, ASR 33, and VLA 27. However, RAC identify VLA 27 with ASR 31 (and IRAS 7). The longest-wavelength points at 3.6 and 6 cm are consistent with the (blackbody) slope obtained for shorter wavelengths, and as such simply removing those points does not strongly affect the fit. From the long-wavelength slope, it seems likely that the object(s) detected at 3.6 and 6 cm are the same as the object(s) detected at 450 and 850 μm, but perhaps it is not the same object as is detected in *JHK*.

We would like at least to place constraints on whether these objects are Class I, II, or III or flat spectrum, based on the 2–10 μm slope. For ASR 31, 32, 33, and 60, the limits on the slopes appear in Table 4; all these objects could be as young as Class I. SK and Knee & Sandell (2000), based on submillimeter observations, classify ASR 33 as a Class I object. Finally, IRAS 7SM2 is not detected at all at short wavelengths, suggesting that it too is deeply embedded.

3.8. *ASR 77 and ASR 111, IRAS 5, SK 26, and SVS 15*

This section combines several isolated sources that we did not detect in *N*. SEDs appear in Figure 10, and best-fit BB temperatures appear in Table 4.

ASR 77 and ASR 111 have detections only on the shorter wavelengths, at best near the peak of the SED. The fits imply both are ~1100 and 1800 K, with luminosities ~0.01 and ~0.1 $L_\odot$, respectively. ASR 77 was classified by ASR as an O or B star. ASR 77 has a 2–10 μm slope of less than 0.8, so it could be as young as Class I. ASR 111, however, has slope less than -0.7, so it is most likely a Class II or III object. Recently, Aspin (2003) derives a BB fit temperature comparable to ours. He concludes that ASR 111 is a late K object, with $T_{\rm eff} \sim 3950$ K, ~0.5 $L_\odot$, ~0.4 $M_\odot$, and ~10^6 yr old. A reddened BB fit at this temperature suggests that $A_v \sim 9$ and that the contribution of the photosphere at *N* is at least 10 times below our upper limit.

There are only three existing detections for IRAS 5. It is apparently a low-temperature object, with best-fit values $\lesssim$50 K; Jennings et al. (1987) only estimate that the temperature is less than 26 K. The fit suggests a large 2–10 μm slope.

SK 26 has only two detections on the long-wavelength tail. Our upper limit constrains this object to be cool, $\lesssim$50 K. Without our upper limit, the slope of the line linking the two detections suggests a much warmer temperature. This object, like IRAS 5, is probably deeply embedded.

Most of the SVS 15 detections are in shorter wavelengths; the VLA point at 3.6 cm is in fact a tentative match. Because this point is at very long wavelengths, it dominates the BB

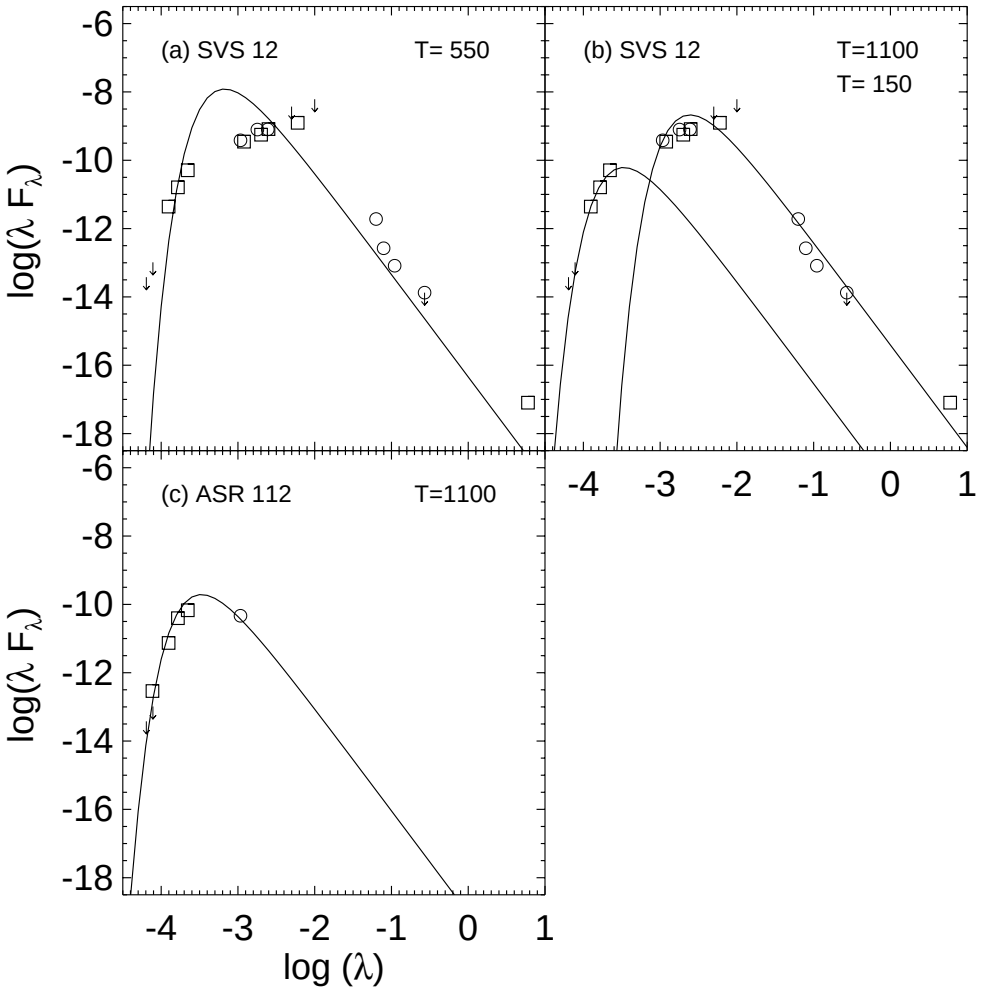

FIG. 7.—SEDs for (*a–b*) SVS 12, and (*c*) ASR 112. (*a*) All the SVS 12 detections, fitting a single blackbody. (*b*) Two-blackbody fit. Cohen & Schwartz (1987) report SVS 12 *IRAS* fluxes at 12, 25, and 60 μm (but not at 100 μm); the 12 and 25 μm detections are essentially identical to our detections reported here and the squares overplotted are very close to the circles representing our detections. Omitting the tentative match with a VLA 6 cm detection does not affect the best-fit temperature. In all panels, detections from the literature are squares, and upper limits (or unapportioned flux) from the literature are arrows. Detections in *N*, 1.1, 0.79, and 0.63 mm presented here are circles; upper limits in *N* or *Qs* are circles with arrows. The line is a simple BB fit; see text. Best-fit temperatures are included in each figure and are listed in Table 4.

fit, and an 1100 K BB does not fit the data including this detection well at all. However, especially since the VLA object is uncertainly linked to SVS 15 and moreover since emission at this wavelength is not thought to arise from thermal processes, we considered the best-fit SED without this point. In this case, the best-fit temperatures rise considerably (to 1450 K BB). The luminosity implied by this fit is $\sim$0.4 $L_{\odot}$. The 2–10 μm slope, -1.4, suggests that it is a Class II or III object. We conclude that the tentative VLA match is in fact incorrect and that this object is a warmer, less embedded object than has been thought. Aspin (2003) derives the same best-fit BB temperature as we do. He assigns this object to be an early K, with $T_{\rm eff} \sim 5000$ K, $\sim$2.5 $L_{\odot}$, $\sim$1.0 $M_{\odot}$, and age $\sim 10^6$ yr. A reddened BB does not fit very well but suggests that $A_v \sim 9$ and that the flux from the photosphere in *N* is a factor of $\sim$3 times below our upper limit.

4. DISCUSSION OF THE ENSEMBLE

By assembling a set of targets that we thought were likely embedded objects, we have by definition created a biased sample. However, the methodology we used for selecting these targets also naturally produces a target list divided into two basic groups of objects: 13 objects detected at wavelengths shorter than $\sim$10 μm and 10 objects detected at longer wavelengths. Only two of these objects (SVS 12 and ASR 33) are detected at both the long and short wavelengths; a third (SVS 15) has a tentative long-wavelength match.

Whether or not an object was detected at *JHK* seems to have had no effect on whether or not we could see it at *N*; five objects previously detected only at (or near) *JHK* were seen in *N*, while six were not seen. Of the eight objects seen only in the long wavelengths, however, only one (IRAS 2a) was seen in *N*. For the three objects with detections across a wide range of wavelengths, one was seen in *N* and two were not, including the object with only a tentative long-wavelength source match. These objects are not well fitted by single blackbodies; our detection and upper limits constrain both these SEDs to be much wider than single BBs.

We attempted observations of only five objects near 20 μm, but there again, whether or not an object was seen at

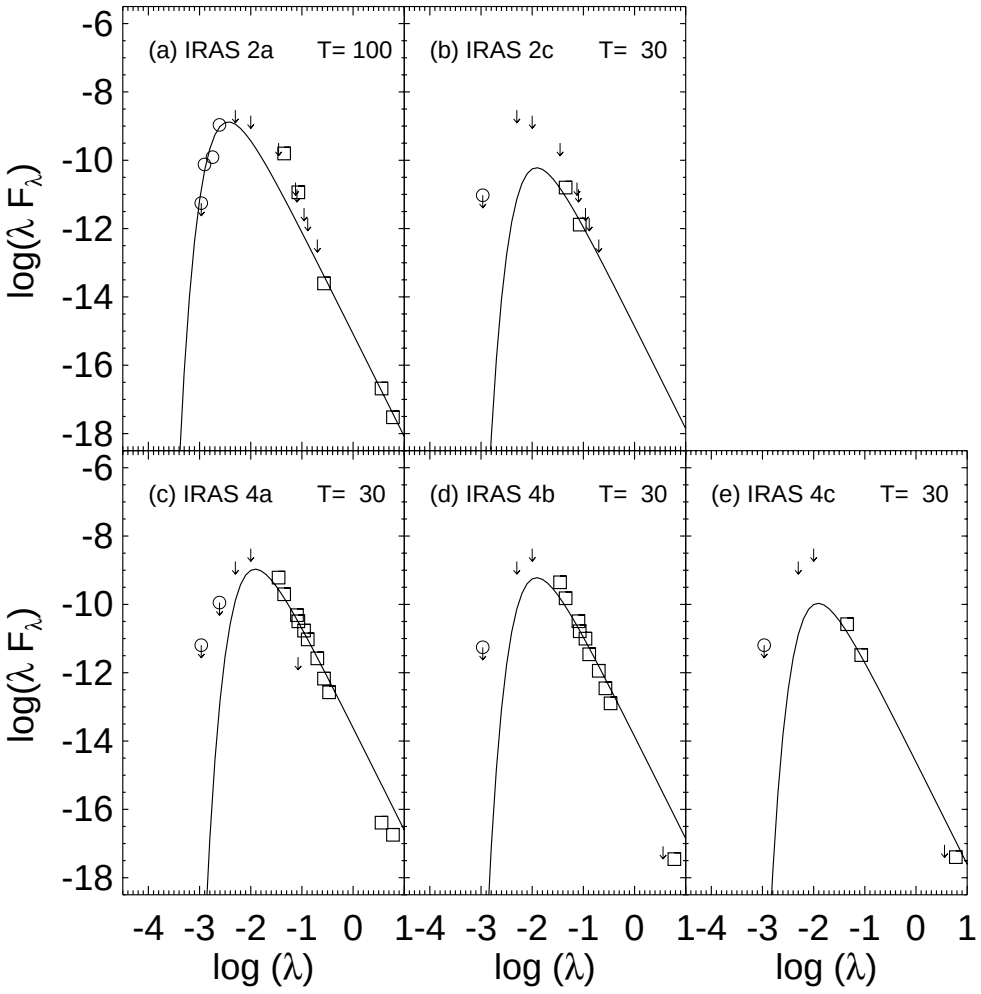

FIG. 8.—SEDs for sources in IRAS 2 and IRAS 4, showing detections from the literature (*squares*), upper limits (or unapportioned flux) from the literature (*arrows*), *N*5, *Q*s, and *Q*5 detections presented here (*circles*), upper limits in *N* and *Q*5 (*circles with arrows*), and simple BB fit (*line*); see text. λ and $\lambda F(\lambda)$ are in cgs units. Best-fit temperatures are included in each figure and are listed in Table 4.

other wavelengths seems to have had no particular effect on whether or not we could see it at 20 μm. In one case, IRAS 2a, the detection at 20 μm defines the SED in a new way for the first time.

As a result of our observations, many objects have new (or different) temperature determinations; of the 21 objects for which detections at more than one wavelength exist, 10 have temperature estimates for the first time or have temperature estimates significantly different than could be assumed from previous detections. For the first time, we are able to classify six objects as Class I–II (or flat spectrum) and place constraints on the classification of 10 more.

Chen et al. (1997) compare the star formation in five molecular clouds. Our survey is extremely biased, and we are unable to determine temperatures in exactly the same way as they did, but we can still compare the fraction of cold sources obtained. Chen et al. define the "cold source fraction" as the fraction of sources with $T < 1000$ K. Our cold source fraction is nearly 60%, certainly reflecting our survey bias toward embedded objects. The largest cold source fraction (and presumably youngest) cluster in Chen et al. is 36%, for Corona Australis. NGC 1333 is thought to be very young, consistent with the age of Corona Australis.

5. SUMMARY

Of the 22 objects we observed with MIRLIN, we were able to detect eight objects for the first time in *N* and/or *Q*. Six of those objects were not detected by *IRAS*, so we have presented the first ever mid-IR detections for those six objects. For the remaining 14 objects, we found upper limits that are useful for constraining the SEDs. On the basis of our detections and upper limits, the previously assumed (or previously unknown) temperatures changed for 10 objects. We are able to classify six objects as Class I–II and place strong constraints on the classification of two more. Most if not all of these objects are likely to be embedded stars; some of these objects are reasonably fitted by reddened photospheres with temperatures derived spectroscopically.

1. Three objects are seen in the field of view that contains only two previously known objects, ASR 107 and ASR 108. One, to the northwest of ASR 107, is an entirely new object. ASR 107 and ASR 108 are both Class II objects.

2. SVS 16 is detected for the first time at *N* and is confirmed to be a close binary. Both the components are classified as flat-spectrum objects. Using spectral classifications to better estimate the temperature of the photosphere, the

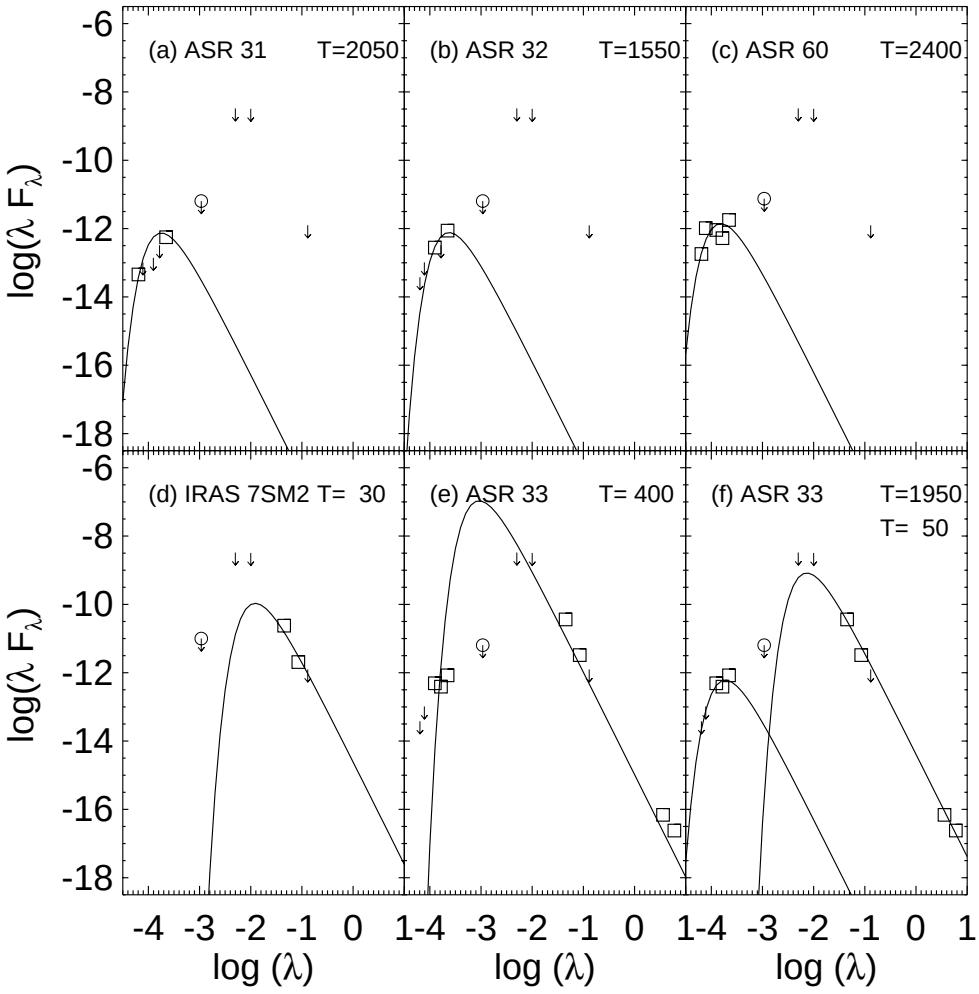

FIG. 9.—SEDs for sources thought to contribute to IRAS 7. showing detections from the literature (*squares*), upper limits (or unapportioned flux) from the literature (*arrows*), upper limits in *N* presented here (*circles with arrows*), and simple BB fit (*line*); see text. λ and $\lambda F(\lambda)$ are in cgs units. Best-fit temperatures are included in each figure and are listed in Table 4.

photospheric contribution to our measured *N* fluxes is only $\sim$10% for both components.

3. SVS 12 is detected for the first time at *N* and previously uncertain observations at broadband *Q* are confirmed via our *Qs* and *Q*5 detections. This object may be extended or a close multiple. It has a peculiar SED that is not easily interpreted, although it is apparently a Class I object. Follow-up observations are warranted.

4. ASR 112 is detected for the first time at *N* and is classified as a flat-spectrum object. Using a spectral classification to better estimate the temperature of the photosphere, the photospheric contribution to our measured *N* flux is only $\sim$10%.

5. IRAS 2a and IRAS 2c were not detected at *N*, but IRAS 2a was detected for the first time in *N*5, *Qs*, and *Q*5. Both these objects are probably quite cool ($\sim$50–100 K).

6. IRAS 4a, 4b, and 4c were not detected at all, and thus all three of these objects are cool and/or embedded ($\lesssim$50 K).

7. None of the five objects associated with IRAS 7 were detected, nor were the isolated objects ASR 77 or IRAS 5. All these objects are cool and/or embedded ($\lesssim$50 K).

8. Although ASR 111 was not detected in *N*, the upper limit, when combined with *JHK* data, constrains it to be a Class II or III object. A reddened blackbody fit to the data constrained by a spectral type suggests that the photospheric contribution at *N* is at least $\sim$10 times below our limit.

9. Although SK 26 was not detected in *N*, our upper limit constrains this object to be quite cool, $\lesssim$50 K.

10. Finally, SVS 15 has been linked in the literature to a VLA source. Our upper limit for this object suggests that it is a warmer, later class (Class II or III), less dusty object than has been previously thought. A reddened blackbody fit to the data constrained by a spectral type suggests that the photospheric contribution at *N* is at least $\sim$3 times below our limit.

NGC 1333 is one of the objects planned for GTO investigations with *SIRTF*. Because *SIRTF* will study the whole region, it will provide a less biased survey of the stars forming in this region.

We wish to acknowledge helpful conversations with A. Muench, G. Sandell, and C. Aspin (who was also our referee). This research has made extensive use of NASA's Astrophysics Data System Abstract Service and of the SIMBAD database, operated at CDS, Strasbourg, France. The

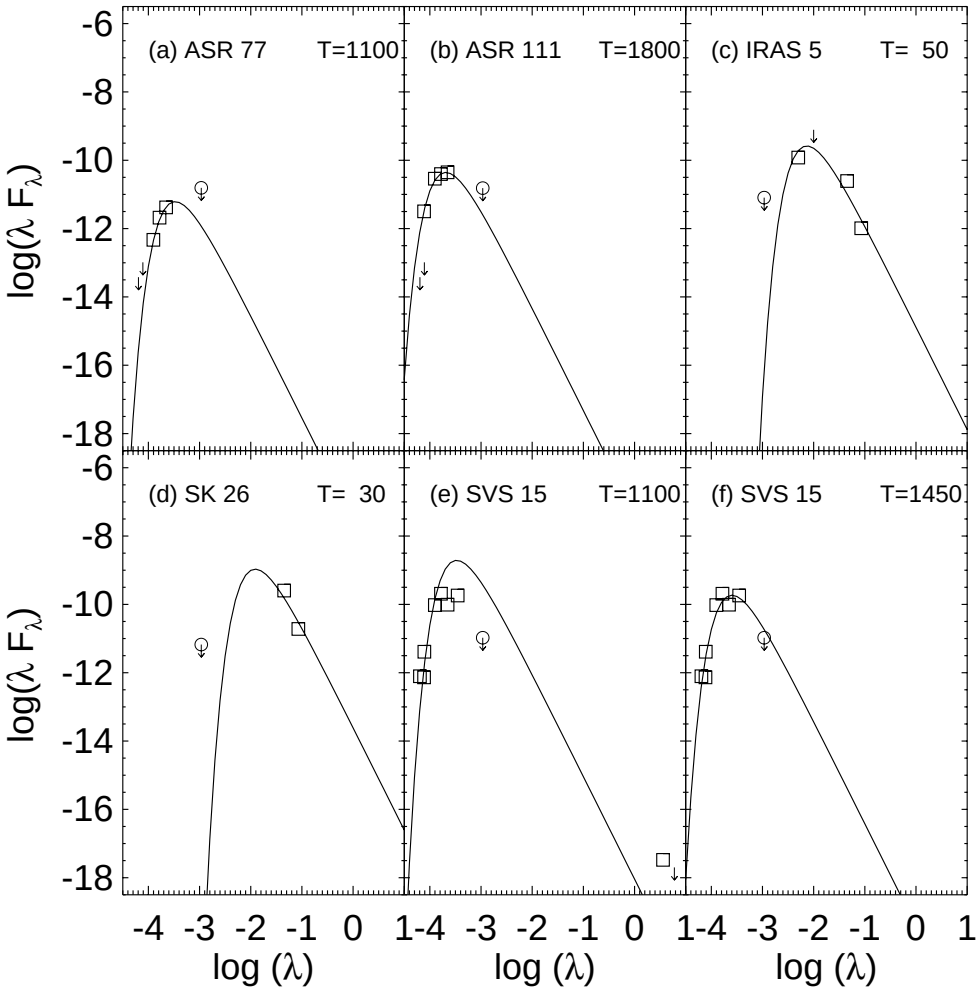

FIG. 10.—SEDs for several isolated sources, showing detections from the literature (*squares*), upper limits (or unapportioned flux) from the literature (*arrows*), *N* detections presented here (*circles*), upper limits in *N* (*circles with arrows*, and simple BB fit (*line*); see text. (*e*) and (*f*) differ only in that the tentative match with a VLA 3.6 cm detection and 6 cm upper limit have been omitted from the fit. λ and $\lambda F(\lambda)$ are in cgs units. Best-fit temperatures are included in each figure and are listed in Table 4.

research described in this paper was carried out at the Jet Propulsion Laboratory (JPL), California Institute of Technology, under contract with the National Aeronautics and Space Administration. Observations at the Palomar Observatory were made as part of a continuing collaborative agreement between Palomar Observatory and JPL. The authors thank the staff at Mount Palomar for their assistance during the observations.

REFERENCES

André, P., Ward-Thompson, D., & Barsony, M. 1993, ApJ, 406, 122
———. 2000, in Protostars and Planets IV, ed. V. Mannings, A. P. Boss, & S. S. Russell (Tucson: Univ. Arizona Press), 59
Aspin, C. 2003, AJ, 125, 1480
Aspin, C., & Sandell, G. 1997, MNRAS, 289, 1
Aspin, C., Sandell, G., & Russell, A. P. G. 1994, A&AS, 106, 165 (ASR)
Bally, J., Devine, D., Alten, V., & Sutherland, R. S. 1997, ApJ, 478, 603
Bally, J., Devine, D., & Reipurth, B. 1996, ApJ, 473, L49
Bally, J., & Reipurth, B. 2001, ApJ, 546, 299
Carpenter, J., Hillenbrand, L., & Skrutskie, M. 2001, AJ, 121, 3160
Carpenter, J., Hillenbrand, L., Skrutskie, M., & Meyer, M. 2002, AJ, 124, 1001
Cernis, K. 1990, Ap&SS, 166, 315
Chen, H., Grenfell, T., Myers, P., & Hughes, J. 1997, ApJ, 478, 295
Choi, M. 2001, ApJ, 553, 219
Cohen, M., & Schwartz, R. 1987, ApJ, 316, 311
Cole, D. M. 2003, in preparation
de Zeeuw, P. T., Hoogerwerf, R., de Bruijne, J. H. J., Brown, A. G. A., & Blaauw, A. 1999, AJ, 117, 354
Getman, K. V., Feigelson, E. D., Townsley, L., Bally, J., Lada, C. J., & Reipurth, B. 2002, ApJ, 575, 354
Harvey, P., Wilking, B., & Joy, M. 1984, ApJ, 278, 156
Jennings, R., Cameron, D., Cudlip, W., & Hirst, C. 1987, MNRAS, 226, 461
Knee, L., & Sandell, G. 2000, A&A, 361, 671
Lada, C., Alves, J., & Lada, E. 1996, AJ, 111, 1964 (LAL)
Lada, C., & Wilking, B. A. 1984, ApJ, 287, 610
Lay, O. P., Carlstrom, J. E., & Hills, R. E. 1995, ApJ, 452, L73
Lefloch, B., Castets, A., Cernicharo, J., Langer, W. D., & Zylka, R. 1998, A&A, 334, 269
Looney, L. W., Mundy, L. G., & Welch, W. J. 2000, ApJ, 529, 477
Marsh, K., Van Cleve, J., Mahoney, M., Hayward, T., & Houck, J. 1995, ApJ, 451, 777
Molinari, S., Liseau, R., & Lorenzetti, D. 1993, A&AS, 101, 59
Motte, F., & André, P. 2001, A&A, 365, 440
Preibisch, T., Neuhauser, R., & Stanke, T. 1998, A&A, 338, 923
Ressler, M., & Barsony, M. 2001, AJ, 121, 1098
Ressler, M. E., Werner, M. W., Van Cleve, J., & Chou, H. A. 1994, Exp. Astron., 3, 277
Rodriguez, L. F., Anglada, G., & Curiel, S. 1999, ApJS, 125, 427 (RAC)
Sandell, G., Aspin, C., Duncan, W. D., Russell, A. P. G., & Robson, E. I. 1991, ApJ, 376, L17
Sandell, G., & Knee, L. B. G. 2001, ApJ, 546, L49 (SK)
Sandell, G., Knee, L. B. G., Aspin, C., Robson, I. E., & Russell, A. P. G. 1994, A&A, 285, L1

Smith, K. W., Bonnell, I. A., Emerson, J. P., & Jenness, T. 2000, MNRAS, 319, 991
Stapelfeldt, K. 1994, in ASP Conf. Ser. 59, Astronomy with Millimeter and Submillimeter Wave Interferometry, ed. M. Ishiguro & W. Welch (San Francisco: ASP), 270
Stapelfeldt, K., Beichman, C., Hester, J., Scoville, N., & Gautier, T. 1991, ApJ, 371, 226
Strom, S. E., Vrba, F. J., & Strom, K. M. 1976, AJ, 81, 314 (SVS)
Wilking, B., Bontemps, S., Schuler, R., Greene, T., & André, P. 2001, ApJ, 551, 357